Featured in Physics

Ultrastrong Unconventional Spin Current via Noncollinear Spin-Orbit Filtering

Hongliang Chen,[1,*] Zi-An Wang,[2,3,*] Xingguo Gao,[4] Hang Zhou,[2,3] Jiaxin Chen,[1] Chang Pan,[5] Lizhu Ren,[6] Qia Shen,[1] Zhenyi Zheng,[7] Dandan Guan,[1,8] Xiaoxue Liu,[1,8] Shiyong Wang,[1,8] Yaoyi Li,[1,8] Hao Zheng,[1,8] Canhua Liu,[1,8] Yumeng Yang,[9] Xuepeng Qiu,[5] Guowei Zhou,[4] Jingsheng Chen,[7] Jinfeng Jia,[1,8] Ding-Fu Shao,[2,†] and Liang Liu[1,8,‡]

[1]*State Key Laboratory of Micro-nano Engineering Science, Tsung-Dao Lee Institute and School of Physics and Astronomy, Shanghai Jiao Tong University, Shanghai 200240, China*
[2]*Key Laboratory of Materials Physics, Institute of Solid State Physics, Hefei Institutes of Physical Science, Chinese Academy of Sciences, Hefei 230031, China*
[3]*University of Science and Technology of China, Hefei 230026, China*
[4]*Key Laboratory of Magnetic Molecules and Magnetic Information Materials of Ministry of Education, School of Chemistry and Materials Science, Shanxi Normal University, Taiyuan, 041004, China*
[5]*Shanghai Key Laboratory of Special Artificial Microstructure Materials and Technology and School of Physics Science and Engineering, Tongji University, Shanghai, 200092, China*
[6]*Department of Electrical and Computer Engineering, National University of Singapore, Singapore, Singapore*
[7]*Department of Materials Science and Engineering, National University of Singapore, 117575, Singapore*
[8]*Hefei National Laboratory, Hefei, China*
[9]*Shanghai Engineering Research Center of Energy Efficient and Custom AI IC, School of Information Science and Technology, ShanghaiTech University, Shanghai 201210, China*

(Received 15 November 2025; revised 2 May 2026; accepted 29 June 2026; published 3 September 2026)

Spin-orbitronics harnesses spin-orbit coupling to generate pure spin currents for energy-efficient information processing, particularly through the spin-orbit torque (SOT) that drives magnetization switching. However, achieving efficient SOT switching of perpendicular magnetization, which is crucial for high-density applications, remains challenging due to the difficulty in generating spin currents with both high conductivity and out-of-plane polarization in conventional, industry-compatible spin sources, such as heavy metals. Here, we overcome this limitation by demonstrating a noncollinear spin-orbit filtering effect at the surface termination of conventional spin sources. This effect selectively transmits electrons based on the relative alignment between their spin vectors and the interfacial Rashba-Edelstein field. By implementing this strategy in platinum (Pt) epitaxial films with (n10) orientations ($n = 2$–4), we achieve exceptionally strong z-polarized spin currents. The resulting out-of-plane spin Hall conductivity reaches a record value of 0.75×10^5 $(\hbar/2e)$ Ω^{-1} m^{-1}, surpassing all previous approaches, and enables robust field-free switching of perpendicular magnetization. Notably, the field-free switching is precisely controlled by engineering the crystal point group symmetry from $C_{1\mathrm{v}}$ to $C_{4\mathrm{v}}$. Our work establishes a general framework for transforming conventional high-symmetry materials into out-of-plane spin sources, paving the way for highly efficient and scalable spintronic memory technology.

DOI: 10.1103/gzp7-1nvx Subject Areas: Condensed Matter Physics, Spintronics

I. INTRODUCTION

Spin-orbit torque (SOT) has become a cornerstone of spintronics, driven by the discovery of efficient charge-to-spin conversion via spin-orbit coupling (SOC) phenomena such as the spin Hall effect (SHE) [1,2] and the Rashba-Edelstein effect (REE) [3,4]. In SOT devices, an in-plane charge current in a spin-source layer generates a transverse, out-of-plane pure spin current that exerts torque on an adjacent magnetic layer to switch its magnetization [5–7]. To date, SOT-based magnetic random-access memory (SOT-MRAM) has been poised to deliver higher switching efficiency, faster operation, and superior endurance,

*These authors contributed equally to this work.
†Contact author: dfshao@issp.ac.cn
‡Contact author: liul21@sjtu.edu.cn

making it a leading candidate for next-generation nonvolatile memory technologies.

For high-density SOT-MRAM integration, perpendicular magnetic anisotropy (PMA) is essential. However, achieving efficient and deterministic SOT switching [8–19] of perpendicular magnetization remains a major challenge, particularly when using conventional, industry-compatible spin-source materials such as Pt [2], Ta [1], and W [20]. These materials exhibit strong spin Hall effects but inherently support only in-plane spin polarization due to their high bulk crystal symmetry [5,21]. As a result, the generated spin torque lacks the necessary out-of-plane (z) component to fully reverse perpendicular magnetization, necessitating an external magnetic field for deterministic switching. To circumvent this limitation, strategies based on low-symmetry materials [22–39] have been explored to introduce z-polarized spin currents. While field-free switching has been demonstrated in some of these systems [24,25,28–32,34–36,39], their spin conductivity, thermal stability, and compatibility with existing semiconductor processes remain limited, hindering scalability and widespread adoption [40].

Here, we pursue a fundamentally different strategy: Rather than searching for new materials, we engineer interfacial terminations in canonical spin sources—materials already known for their high spin Hall conductivity (SHC), chemical robustness, and CMOS compatibility. At the interface, a noncollinear spin-orbit filtering effect emerges, whereby electron transmission depends on the orientation of the electron's spin relative to the interfacial Rashba-Edelstein field, enabling efficient generation of strong z-polarized spin currents. Using Pt films with specific (n10) orientations ($n = 2$–4) as a prototype, we achieve a record out-of-plane spin Hall conductivity of 0.75×10^5 $(\hbar/2e)$ $\Omega^{-1}\,\mathrm{m}^{-1}$ and demonstrate robust, field-free switching of perpendicular magnetization without external assistance. Our work demonstrates that bulk crystal symmetry does not impose a fundamental limit on spin current polarization: When interfacial quantum transport is properly engineered, conventional materials can surpass exotic alternatives in both functionality and performance. This principle establishes a scalable route to high-efficiency spintronic devices based on industry-standard materials, with direct implications for next-generation memory technologies.

II. RESULTS AND DISCUSSION

A. Noncollinear spin-orbit filtering effect

The net polarization of a spin current is determined by the ensemble spin expectation value of all participating electrons. In heavy metals with strong SOC, where spin is not a conserved quantity, individual electrons can possess spin components along arbitrary directions, although a high crystal symmetry typically enforces cancellation of components nonorthogonal to the charge and spin current directions. This phenomenon is exemplified by conventional spin sources such as cubic Pt, in which an isotropic spin conductivity tensor ensures that an x-directional charge current always generates a purely y-polarized out-of-plane spin current regardless of the crystallographic orientation. Consequently, despite their superior advantages, these conventional spin sources are unsuitable for deterministic perpendicular magnetization switching according to conventional wisdom. Here, we propose a way to circumvent this fundamental symmetry constraint of conventional spin sources (e.g., Pt) at interfacial terminations through noncollinear spin-orbit filtering, which is a general spin-selection mechanism where electron transmission depends on the relative orientation between the spin vector of an electron ($\hat{\boldsymbol{n}}$) and the interfacial effective field generated by the Rashba-Edelstein effect ($\boldsymbol{u_R}$). Unlike conventional spin filtering, in which only parallel or antiparallel alignments of $\hat{\boldsymbol{n}}$ and $\boldsymbol{u_R}$ are considered [41,42], our mechanism accounts for arbitrary $\hat{\boldsymbol{n}}$ orientations: Transmission is maximized when $\hat{\boldsymbol{n}} \| \boldsymbol{u_R}$, monotonically reduced for noncollinear orientations, and strongly suppressed as $\hat{\boldsymbol{n}}$ approaches antiparallel alignment with $\boldsymbol{u_R}$ (see Supplemental Material for details [43], which includes Refs. [44–56]). This effect significantly suppresses the cancellation of spin components that would otherwise be nonorthogonal to the charge and spin current directions in the bulk. Consequently, unconventional z-polarized currents are generated through this angular selection process.

This effect can be intuitively illustrated by contrasting high- and low-symmetry terminations. In the Pt (100) film shown in Fig. 1(a), an x-directional charge current J_c generates orthogonal spin currents J_{s1} (y directional with z spin) and J_{s2} (z directional with y spin) that encounter purely in-plane $\boldsymbol{u_R}$ at the high-symmetry termination, preserving the original polarization, as shown in Fig. 1(a). The situation dramatically changes in Pt (n10) films ($n > 1$), which can be conceptualized as Pt (100) rotated around the [001] axis, as shown in Fig. 1(b). Here, both spin currents adopt oblique propagation directions with mixed polarizations. As represented by Pt (210) in Figs. 1(c) and 1(d), the interfacial termination reduces the symmetry to the C_{1v} point group, retaining only a mirror symmetry about the [001] axis. This reduced symmetry permits finite z components in $\boldsymbol{u_R}$, enabling strong filtering of misaligned J_{s1} and leaving dominantly J_{s2} to contribute z polarization to the emitted current, as shown in Fig. 1(b). To further validate noncollinear spin filtering, we perform first-principles calculations based on a Pt (210) slab model. The results reveal that the low-symmetry Pt (210)/Ti interface naturally hosts a momentum-dependent spin-orbit field with a finite out-of-plane component. This finding supports the emergence of unconventional spin currents at high-index Pt/Ti interfaces when the applied electric field is not parallel to the mirror plane (see Sec. IV and Supplemental Material for details [43]).

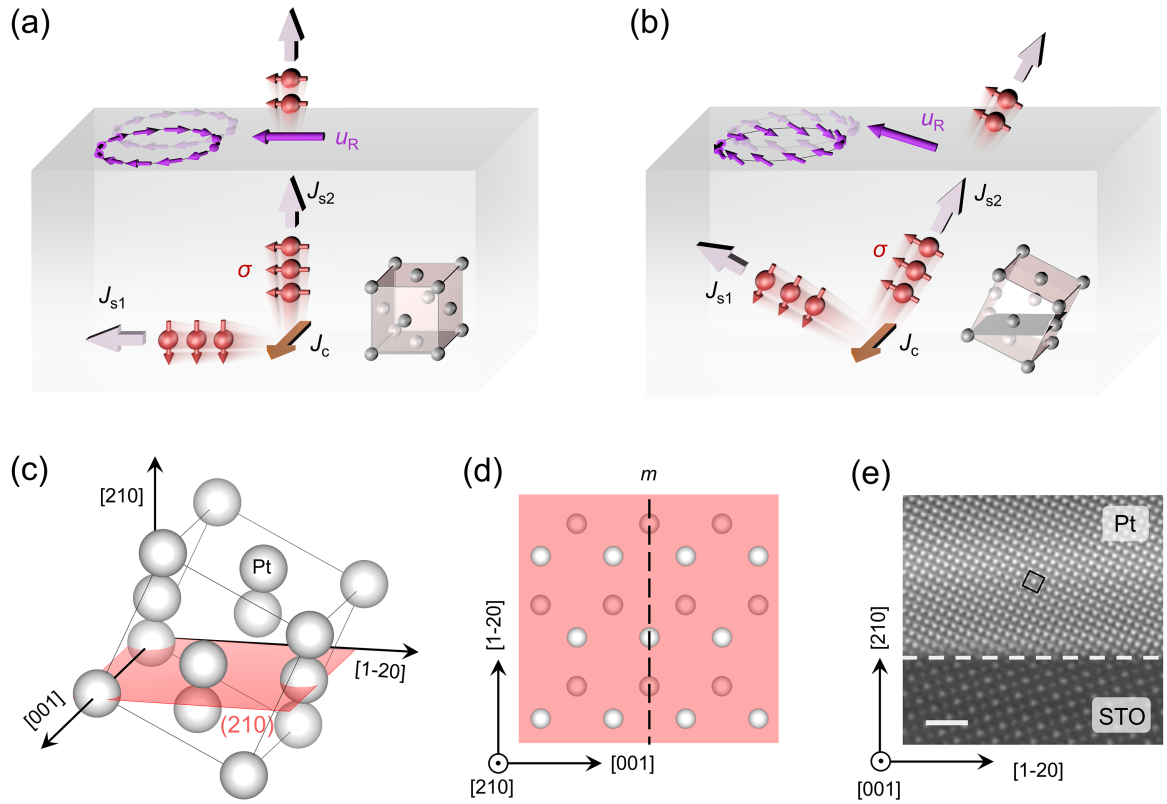

FIG. 1. Noncollinear spin-orbit filtering effect in conventional spin sources. Schematics of spin-orbit filtering effect at high-symmetry (100) (a) and low-symmetry (210) (b) interfaces, respectively. The purple arrows (denoted as "$\boldsymbol{u_R}$") represent the Rashba-Edelstein effective field contributed by the momentum-dependent spin textures from Pt (100) and Pt (210) interfacial terminations. Compared with Pt (100), Pt (210) has a z-tilted spin-orbit field when current is applied perpendicularly to the mirror plane. In Pt (100) (a), an x-directional charge current J_c generates orthogonal spin currents J_{s1} (y directional with z spin) and J_{s2} (z directional with y spin) that encounter purely in-plane $\boldsymbol{u_R}$ at the high symmetric termination, preserving the original polarization. Pt (210) (b) can be conceptualized as rotated Pt (100) around the [001] axis, where J_{s1} and J_{s2} adopt oblique propagation directions with mixed polarizations. The tilted $\boldsymbol{u_R}$ in this case enables strong filtering of misaligned J_{s1}, leaving J_{s2} to dominantly contribute z polarization to the emitted current. (c) The (210) plane in fcc Pt crystal structure. (d) Top view of the Pt (210) plane. The dashed line represents the mirror plane ("m"). The white and red balls represent two adjacent Pt atomic layers (white on top and red below) projected in the (210) orientation. (e) High-angle annular dark-field-scanning transmission electron microscopy (HAADF-STEM) image of 6-nm Pt thin film deposited on (210)-oriented $SrTiO_3$. The tilted dark square represents a unit cell of fcc Pt, and the scale bar is 1 nm.

B. Field-free switching of perpendicular magnetization

To confirm our hypothesis that z-polarized spin currents can be generated in Pt films with low-symmetry terminations, we first deposit Pt thin films on a (210)-oriented $SrTiO_3$ (STO) substrate by magnetron sputtering (see Sec. IV). X-ray diffraction (XRD) (Supplemental Material [43]) and cross-sectional high-angle annular dark-field scanning transmission electron microscopy (HAADF-STEM), shown in Fig. 1(e), confirm the high-quality epitaxial growth of (210)-oriented fcc Pt with high crystallinity and an atomically sharp interface. After depositing the Pt (210) film, we sequentially deposit a multilayer stack of Ti (2 nm)/CoFeB(1 nm)/MgO(10 nm)/Ta(2 nm), which is used to probe the spin current generated by Pt. The HAADF-STEM image of the Pt/Ti/CoFeB/MgO/Ta structure exhibits well-defined interfaces (Supplemental Material [43]), with layer thicknesses matching their nominal values. For simplicity, we refer to this stack as "Pt/FM" in subsequent discussions. The Pt/FM is then patterned into 5 μm Hall bar devices as shown in Fig. 2(a), with the charge current angle (φ_I) varied relative to the [001] direction in the Pt (210) plane shown in Fig. 2(b). Anomalous Hall effect (AHE) loops measured at $\varphi_I = 0°$ and other angles [shown in Fig. 2(c) and Supplemental Material [43]] confirm the perpendicular magnetic anisotropy (PMA) of the samples. The AHE amplitude (ΔR_H) remains nearly constant across all angles (Supplemental Material [43]). Next, we apply electrical current pulses (I_{pulse}) to switch the magnetization (see Method) in the absence of an external magnetic field, and the result is shown in Fig. 2(d), where an anisotropic switching behavior on φ_I is observed. Deterministic magnetization switching occurs at most angles except for $\varphi_I = 90°$ and 270°, where the current is applied parallel

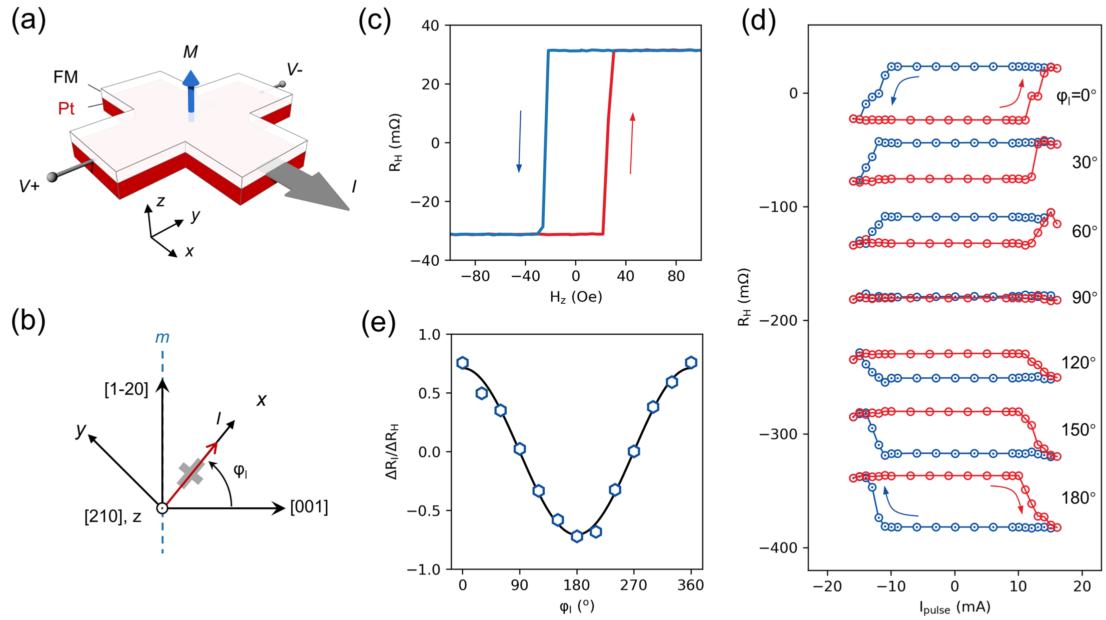

FIG. 2. Current-induced field-free magnetization switching in a Pt/ferromagnet heterostructure with C_{1v} symmetry. (a) Schematic of the Pt (210)/FM Hall device for electrical transport measurements. "FM" represents the ferromagnetic layer with a Ti (2 nm)/CoFeB(1 nm)/MgO(10 nm)/Ta(2 nm) stack. (b) Definition of the current-flowing direction (φ_I). The current (I) is applied along the x direction of the Hall bar (gray cross). The blue dashed line represents the mirror plane ("m"). (c) Anomalous Hall resistance vs H_z for $\varphi_I = 0°$. (d) Angle dependence of current-induced magnetization switching. The switching loops are vertically shifted for clarity. The switching current density in the Pt layer is around 2.5×10^7 A/cm^2. (e) Switching ratio as a function of φ_I and fitting curve using a cosine function.

to the mirror plane. The amplitude of the switched Hall resistance (ΔR_I) is maximized at $\varphi_I = 0°$ and 180° with opposite switching polarities (indicated by arrows), where the current is applied perpendicular to the mirror plane. The switching ratio ($\Delta R_I/\Delta R_H$) follows a $\cos\varphi_I$ dependence [Fig. 2(e)], exhibiting a onefold angular dependence that matches the C_{1v} crystal symmetry of Pt (210). In a control sample where the Pt layer is removed from the stack, no switching is observed, indicating that the Ti layer alone cannot induce field-free switching (Supplemental Material [43]). When the growth temperature of Pt is decreased from 550 °C to 200 °C, field-free switching can still be achieved (Supplemental Material [43]). We note that the incomplete switching ($\Delta R_I/\Delta R_H < 80\%$) in Fig. 2(d) is due to the pinning effect from Hall voltage arms. By fabricating the ferromagnetic layer into a round pillar above the Pt layer, near-complete switching (over 98%) is observed, as further confirmed by magneto-optical Kerr effect (MOKE) imaging (Supplemental Material [43]).

To further investigate the noncollinear spin-orbit filtering effect, we prepare Pt films with (010), (110), (210), (310), and (410) surface terminations, whose top views are shown in Figs. 3(a)–3(e), respectively. The growth conditions for (010)-, (110)-, (310)-, and (410)-oriented Pt/FM are identical to those for Pt (210)/FM (see Sec. IV). The resistivity of these Pt (n10) films remains almost constant (~3.1–3.2 × 10^{-7} Ωm), as shown in the Supplemental Material, Fig. S12 [43]. These Pt (n10)-based samples ($n = 0$–4) exhibit comparable saturation magnetization (M_s), while their anisotropic field (H_k) increases with increasing n from 0 to 4 (Supplemental Material [43]). Structurally, Pt (410), (310), and (210) share the same C_{1v} symmetry (featuring only one mirror plane), which supports a tilted $\boldsymbol{u_R}$ when the current is not parallel to the mirror plane. In contrast, Pt (110) exhibits C_{2v} symmetry (two mirror planes + C_2 axis), and Pt (010) [or, equivalently, Pt (100) in Fig. 1(a)] has C_{4v} symmetry (four mirror planes + C_4 axis), both of which restrict $\boldsymbol{u_R}$ to in-plane orientations regardless of the current direction. Figure 3(k) illustrates these planes within the Pt cubic structure. For switching measurements, the current pulse direction is fixed along the [001] direction for all the samples. As shown in Figs. 3(f)–3(j), field-free switching is observed in the Pt (210)-, Pt (310)-, and Pt (410)-based devices but is absent for the Pt (010) and Pt (110) devices, suggesting that the highest symmetry permitting field-free switching is a single mirror plane. When an external magnetic field (H_x) of ±50 Oe is applied, all five devices exhibit deterministic switching with identical polarities, consistent with conventional field-assisted SOT switching. The decrease in Hall resistance at the highest current values is mainly due to Joule-heating-induced demagnetization, which does not affect the eventual switching ratio. The H_x dependence of the switching ratio $\Delta R_I/\Delta R_H$ [Fig. 3(l)] is extracted

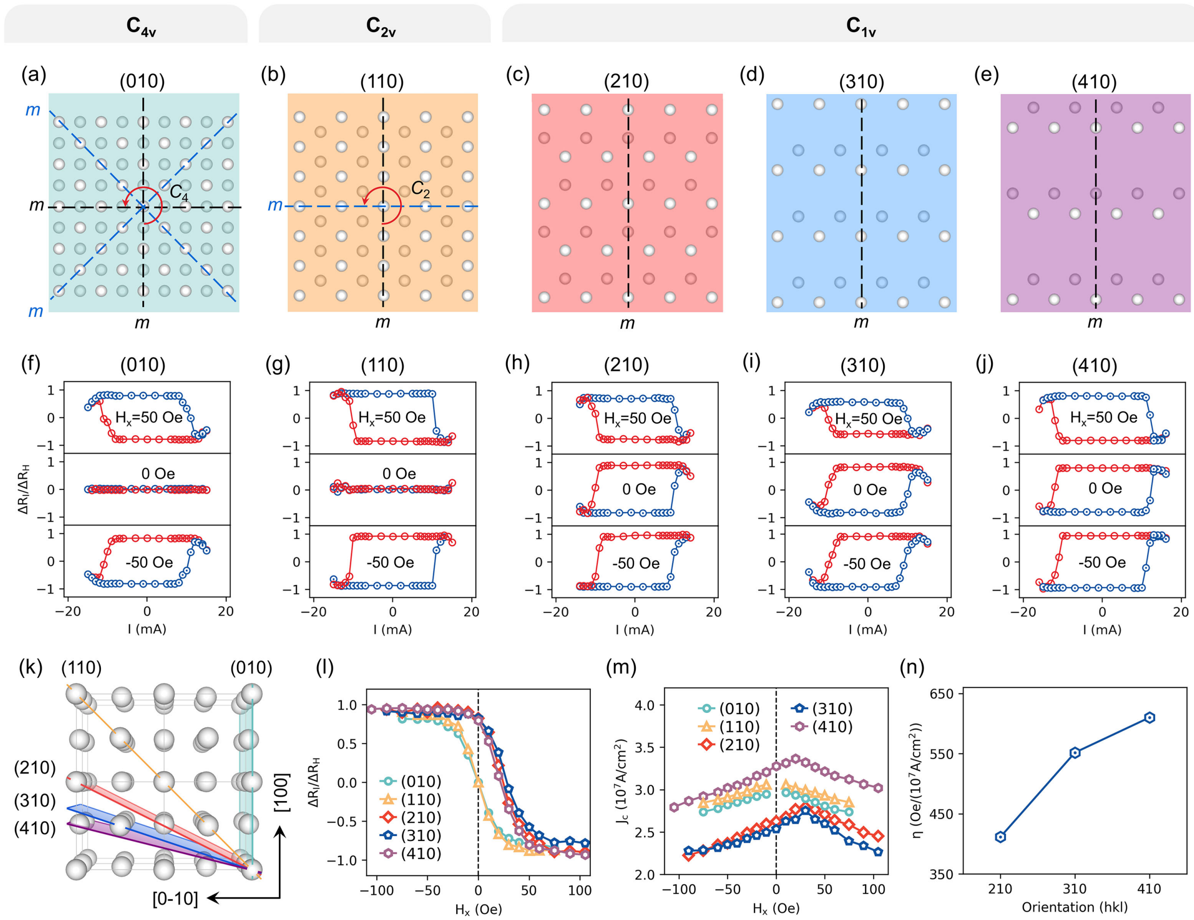

FIG. 3. Controlling spin-orbit torque switching via point group symmetry. (a)–(e) Top view of the Pt (010), (110), (210), (310), and (410) planes, which exhibit three different symmetries of C_{4v}, C_{2v}, and C_{1v}. The mirror symmetry is denoted as "m," and the twofold and fourfold rotational symmetries are denoted as C_2 and C_4, respectively. (f)–(j) Current-induced magnetization switching in Pt $(n10)$/FM samples with $n = 0$, 1, 2, 3, and 4 under external magnetic fields of $H_x = 50$, 0, and -50 Oe. (k) Five typical $(n10)$ lattice planes in the fcc Pt crystal structure. (l) H_x dependences of switching ratio ($\Delta R_{\mathrm{I}}/\Delta R_{\mathrm{H}}$) and (m) switching current density (J_c) for Pt $(n10)$/FM samples. (n) SOT switching efficiency ($\eta = H_k/J_c$) under zero magnetic field for the Pt (210)-, (310)-, and (410)-based heterostructures.

from the switching loops for the five devices obtained under various H_x values (Supplemental Material [43]). The Pt (010) and Pt (110) devices exhibit an antisymmetric $\Delta R_{\mathrm{I}}/\Delta R_{\mathrm{H}} - H_x$ relationship, with a near-zero switching ratio at $H_x = 0$. In contrast, the curves of the Pt (210), Pt (310), and Pt (410) devices are laterally shifted (~23–28 Oe rightwards), achieving a nearly complete magnetization switching at $H_x = 0$. Figure 3(m) summarizes the switching current density (J_c) versus H_x. For Pt (010) and Pt (110), J_c decreases with increasing $|H_x|$, peaking near $H_x = 0$. In contrast, for Pt (210), Pt (310), and Pt (410), the maximum J_c occurs at 20 to 30 Oe, consistent with the shifted fields in Fig. 3(l). Within a monodomain model, the SOT switching efficiency (neglecting Joule heating) is defined as [57] $\eta = H_k/J_c$. As shown in Fig. 3(n), η increases from 410 Oe/(10^7 A/cm^2) to 610 Oe/(10^7 A/cm^2) as n increases from 2 to 4, demonstrating the tunability of the field-free switching efficiency through surface symmetry engineering of Pt.

C. Characterization of out-of-plane spin

To quantify the spin polarization associated with the noncollinear spin-orbit filtering, we first measure the current-induced out-of-plane (OOP) effective field (H_{OOP}). Note that H_{OOP} is estimated from the anomalous Hall loop shifts under positive and negative current pulses [8,58]. Taking the Pt (210)/FM device as an example, application of $I_{\mathrm{pulse}} = 13$ mA (-13 mA) at $\varphi_{\mathrm{I}} = 0°$ produces leftward (rightward) loop shifts [Fig. 4(a)], corresponding to a positive (negative) H_{OOP}. The effective was calculated as follows: $H_{\mathrm{OOP}} = (H_{\mathrm{right}} - H_{\mathrm{left}})/2$, where H_{right} and H_{left} denote the central fields of the loops under positive and negative I_{pulse}. The current dependences of H_{OOP} for the Pt (210) device at $\varphi_{\mathrm{I}} = 0°$, 90°, and 180° are shown in Fig. 4(b). For $\varphi_{\mathrm{I}} = 0°$, H_{OOP} remains nearly zero below a

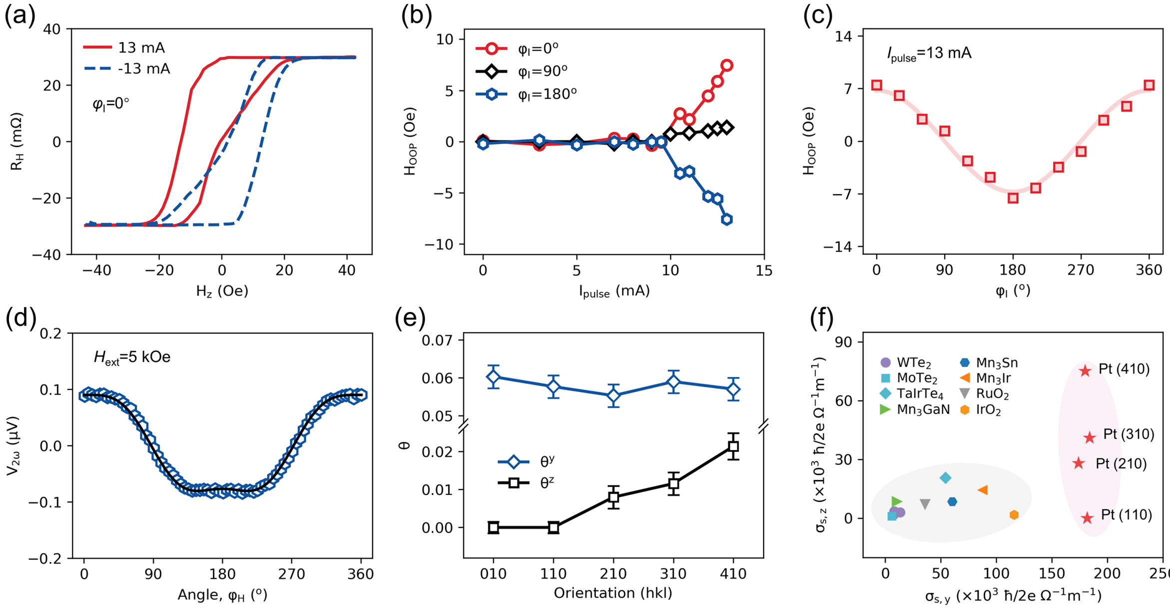

FIG. 4. Spin Hall conductivity in (n10)-oriented Pt and existing low-symmetry materials. (a) Anomalous Hall loops of the Pt (210)/FM device at $\varphi_I = 0°$ under +13 mA (red solid line) and −13 mA (blue dashed line) pulsed currents. (b) Current-induced OOP effective field of the Pt (210)/FM device as a function of the pulsed current for $\varphi_I = 0°$ (red), $\varphi_I = 90°$ (black), and $\varphi_I = 180°$ (blue). (c) OOP effective field H_{OOP} of the Pt (210)/FM device at $I_{pulse} = 13$ mA. The solid line represents a cosine fit. (d) Second harmonic Hall voltages of the Pt (210)/FM device at $\varphi_I = 0°$ as a function of the in-plane magnetic field angle (φ_H) under $H = 5$ kOe. The solid line is a fit using Eq. (1). (e) Pt surface orientation dependence of the charge-to-spin conversion efficiency (θ^y and θ^z) for the y spin and z spin. (f) OOP and in-plane SHCs summarized for other low-symmetry materials and Pt (n10) ($n = 1, 2, 3, 4$) in this work. The references for the SHC of other materials are listed in the Supplemental Material, Table S1 [43].

threshold current of 9.5 mA before rising to 7.5 Oe at 13 mA. For $\varphi_I = 180°$, the threshold current is the same as that for $\varphi_I = 0°$, but H_{OOP} exhibits opposite polarity. For $\varphi_I = 90°$, H_{OOP} stays near zero across all currents. The opposite signs of H_{OOP} for $\varphi_I = 0°$ and 180° correspond to reversed switching polarities in Fig. 2(d), whereas the near-zero H_{OOP} at $\varphi_I = 90°$ accounts for the absence of field-free switching. The threshold behavior in the H_{OOP}-I_{pulse} relation aligns with reports on z-spin induced switching [15,25], where SOT modulates the effective damping (see Supplemental Material [43]). Figure 4(c) presents the φ_I dependence of H_{OOP} measured at $I_{pulse} = 13$ mA (see raw data in Supplemental Material Fig. S15 [43]). Similar to $\Delta R_I/\Delta R_H$-φ_I in Fig. 2(e), H_{OOP}-φ_I also exhibits a onefold angular dependence, which directly correlates the generated z spin with the z component of $\boldsymbol{u_R}$ in Fig. 1(b).

Second harmonic Hall voltage measurements are performed to further quantify the spin polarizations in the y and z directions [22,30,59]. An in-plane magnetic field (H_{ext}) exceeding the saturation field is applied, while a small ac current (I_{ac}) is applied to drive magnetization oscillation, generating a second harmonic Hall voltage ($V_{2\omega}$) via the SOT effect (see Supplemental Material for details [43]). By rotating the in-plane angle (φ_H) of H_{ext}, the $V_{2\omega}$ signal follows [22,59],

$$V_{2\omega} = \left(\frac{V_{AHE}}{2}\frac{H_{DLy}}{H_{ext} - H_K} + V_{ther}\right)\cos\varphi_H + \left(V_{PHE}\frac{H_{FLy} + H_{Oe}}{H_{ext}}\right)\cos(2\varphi_H)\cos\varphi_H + V_{PHE}\frac{H_{DLz}}{H_{ext}}\cos(2\varphi_H) \quad (1)$$

where V_{AHE} and V_{PHE} represent the anomalous Hall voltage and planar Hall voltage, respectively. Here, H_{DLy} (H_{FLy}) is the dampinglike (fieldlike) effective field originating from the y spin, H_{DLz} is the dampinglike effective field originating from the z spin, and H_{Oe} represents the Oersted field. For the Pt (210)/FM device at $\varphi_I = 0°$, the $V_{2\omega} - \varphi_H$ relation under $H_{ext} = 5$ kOe is shown in Fig. 4(d), from which we can derive the parameters $A = (V_{AHE}/2)(H_{DLy}/H_{ext} - H_K) + V_{ther}$ and $C = V_{PHE}(H_{DLz}/H_{ext})$ according to the fit with Eq. (1) (see Supplemental Material for the fitting procedure [43]). By measuring A and C at various H_{ext} values, we obtain H_{DLz} and H_{DLy}. As expected for spin-orbit torques, the extracted H_{DLz} scales linearly with the applied current (see Supplemental Material, Fig. S23 [43]). For Pt (210)/FM, the spin-torque efficiencies H_{DLz}/J and H_{DLy}/J are estimated to be 2.8 Oe/(10^7 A/cm^2) and 16.9 Oe/(10^7 A/cm^2), respectively. Note that J is the current density flowing in the Pt layer. For comparison, we measure H_{DLz}/J and H_{DLy}/J for Pt (010)-, Pt (110)-, Pt (310)-, and Pt (410)-based heterostructures, and the results are shown in the Supplemental Material, Fig. S24 [43]. Here, H_{DLz}/J is negligible for the high-symmetry Pt (010) and Pt (110) surfaces but increases with n from 2 to 4 in the low-symmetry Pt (n10) surfaces. In contrast, the y-spin-related H_{DLy}/J fluctuates [$\sim$16–19 Oe/(10^7 A/cm^2)] across the orientations, indicating that the orientation does not greatly affect the in-plane spin torque efficiency. In accordance with the established method [2,60], we calculate the charge-to-spin conversion efficiency (θ^y, θ^z) for the y spin and z spin using the formula $\theta = (2eM_S t_{\mathrm{FM}}/\hbar)(\mu_0 H/J)$ with H_{DLy}/J and H_{DLz}/J, and their orientation dependences are shown in Fig. 4(e). The obtained θ^y value is in the range of 0.055–0.060, consistent with previous reports on epitaxial Pt [61,62]. In contrast, θ^z is calculated to be 0.009, 0.013, and 0.024 for Pt (210)-, Pt (310)-, and Pt (410)-based samples, respectively. A similar trend is observed in the orientation dependence of H_{OOP} on the Pt (n10), as shown in the Supplemental Material, Fig. S17 [43]. We further investigate the H_{DLz} strength for different Pt (n10) orientations using a thicker CoFeB layer with in-plane magnetic anisotropy (IMA) in Pt/CoFeB/MgO/Ta devices (without Ti). We note that the removal of the Ti layer does not alter the results (Supplemental Material, Fig. S26). We compare θ^z of IMA samples with that of PMA samples and observe similar trends across different Pt (n10) crystal textures (see Supplemental Material, Fig. S27 [43]). By using θ^y and θ^z, we derive the SHC for the y spin and z spin via $\sigma_{s,y} = (\hbar/2e)\theta^y\sigma_c$ and $\sigma_{s,z} = (\hbar/2e)\theta^z\sigma_c$, where σ_c represents the conductivity of the Pt films (~ 3.1–$3.2 \times 10^6\ \Omega^{-1}\ \mathrm{m}^{-1}$ for the five orientations). Figure 4(f) summarizes the $\sigma_{s,y}$ and $\sigma_{s,z}$ values for various low-symmetry systems (including WTe_2 [22], $MoTe_2$ [37], $TaIrTe_4$ [28], Mn_3GaN [23], Mn_3Ir [34], RuO_2 [26], and IrO_2 [27]) and our Pt (n10) systems ($n = 1,\ 2,\ 3,\ 4$). Notably, Pt (410) achieves $\sigma_{s,z} \sim 0.75 \times 10^5\ \hbar/2e(\Omega\,\mathrm{m})^{-1}$, the highest reported value thus far, while maintaining a large $\sigma_{s,y}(\sim 1.8 \times 10^5\,\hbar/2e(\Omega\mathrm{m})^{-1})$ at the same time. The increasing trend of $\sigma_{s,z}$ with n from 2 to 4 is consistent with the switching efficiency evolution in Fig. 3(n), suggesting that Pt (410) may possess a suitable $\sigma_{s,y}/\sigma_{s,z}$ ratio that optimizes the switching performance.

Having observed the z-polarized spin-current-induced field-free magnetization switching, we employe the MOKE imaging to visualize the reversal process. It is found that the deterministic switching proceeds via domain nucleation and domain-wall (DW) propagation (see Supplemental Material [43]). In conventional high-symmetry spin Hall materials, efficient DW motion relies on y-polarized spin currents and Néel-type walls stabilized by a large interfacial Dzyaloshinskii-Moriya interaction (DMI) [63–65]. However, in our Pt/Ti/CoFeB system, the measured DMI effective field is only about 30–33 Oe (Supplemental Material, Fig. S31), much smaller than typical Pt/FM systems [58,66], indicating that the 2-nm Ti interlayer strongly suppresses interfacial DMI [67,68]. Under such weak DMI, the DW configuration is not rigidly locked to a Néel state and may exhibit Bloch-type character [65,69,70]. In this context, a z-polarized spin current can generate an out-of-plane torque $\tau_z \propto \boldsymbol{m} \times (\boldsymbol{m} \times \hat{z})$ (where $\boldsymbol{m}$ is the DW center moment), which can drive in-plane DW moments toward the z direction regardless of DW type. This result suggests that DW-mediated switching is not strictly constrained by the requirement of homochiral Néel walls, providing a pathway for field-free magnetization reversal.

III. SUMMARY AND PERSPECTIVE

We expect that the strategy we demonstrated in this work could offer a paradigm shift for spin orbitronics. While z-polarized spin currents have previously been pursued in materials with low bulk symmetry, such systems often suffer from poor CMOS compatibility, high electrical resistivity, and low spin conductivity, limiting their practical utility in integrated spintronic devices. In contrast, our approach only requires the presence of an interface termination that offers noncollinear spin-orbit filtering and thus is highly versatile and broadly applicable. Beyond Pt, we anticipate that the widely used spin sources—such as W, Ta, and many more sources already known for their excellent CMOS process compatibility and high spin Hall efficiency—can also leverage this mechanism to generate strong z-polarized spin currents. Furthermore, while epitaxial growth along nonprincipal crystallographic orientations [e.g., Pt (n10)] provides one route to generate the required interface termination, we envision that even polycrystalline films could achieve similar effects by inserting a two-dimensional (2D) material as a spacer between the spin source and the ferromagnetic layer. Such a 2D layer could locally break inversion symmetry and induce $\boldsymbol{u_R}$ with finite out-of-plane components, enabling noncollinear filtering for the spin current generated by polycrystalline spin sources.

In summary, we revealed the hidden potential of Pt, which is the most widely used spin current source, by demonstrating efficient out-of-plane spin generation via a noncollinear spin-orbit filtering mechanism at its high-index facets. This mechanism enables field-free switching of perpendicular magnetization in Pt (210)-, Pt (310)-, and Pt (410)-based systems, with a record-high z-polarized SHC value that underscores its exceptional efficiency. Our findings fundamentally reshape our understanding of conventional spin sources: The bulk crystal symmetry need not dictate unconventional spin-dependent transport, and properly engineered terminations can transform existing materials into platforms for realizing unprecedented functionality. This shift from material discovery to interface control creates opportunities for implementing energy-efficient spintronic memory using foundry-compatible materials, including but not limited to heavy metals and their alloys.

IV. METHODS

A. Sample growth and device fabrication

Pt (6-nm) films were epitaxially deposited on $SrTiO_3$ (010), (110), (210), (310), and (410) single-crystal substrates by dc magnetron sputtering (AJA Orion 8). Before deposition, the $SrTiO_3$ substrate was heated to 550 °C and held at this temperature for 1 h. For the deposition of the 6-nm Pt film, the Ar pressure was 1.5 mTorr, and the temperature was 550 °C. The sputtering power was 20 W, with a deposition rate of 0.032 nm/s. After deposition, the Pt film was annealed *in situ* at 550 °C for 1 h and then naturally cooled to room temperature in a vacuum environment. Ti (2 nm), CoFeB (1 nm), MgO (10 nm), and Ta (2 nm) were deposited on the Pt film at room temperature and annealed at 190 °C for 5 min. Afterwards, the Pt/Ti/CoFeB/MgO/Ta stack was patterned into 5-μm Hall bars with different in-plane orientations using a laser writer and Ar ion milling.

B. Scanning transmission electron microscope (STEM)

STEM samples were fabricated with a focused ion beam (FIB, ZEISS Crossbeam 350). The sample was thinned down using a Ga ion beam first, with an accelerating voltage of 30 kV. Afterwards, the sample was polished with a 2-kV ion beam. Structure characterization was conducted with a Spectra 300 STEM (Thermo Fisher Scientific) equipped with an X-CFEG and the S-CORR probe aberration corrector operating at an accelerating voltage of 300 kV. HAADF images were acquired with a probe forming angle of 30 mrad and a collection angle of 46–200 mrad.

C. Current-induced switching measurement

In the current-induced magnetization switching measurement, for each data point, a pulsed dc electrical current with a duration of 30 μs was applied. After 7 seconds, the Hall resistance was recorded by using a small ac excitation current (100–200 μA).

D. First-principles calculations

To model the Pt/Ti interface relevant to the experiment, we constructed a slab model based on a Pt (210) supercell separated by a vacuum region. The slab contained 11 atomic layers, and the Pt atoms in the topmost layer were replaced by Ti atoms to mimic the Pt/Ti interfacial termination. This model was intended to capture the local inversion-symmetry breaking and reduced surface symmetry at the Pt/Ti interface. The electronic structure was calculated within density functional theory using the QUANTUM ESPRESSO package [71], with fully relativistic pseudopotentials [72] to include spin-orbit coupling self-consistently and the Perdew-Burke-Ernzerhof generalized-gradient approximation [73] for the exchange-correlation functional. A plane-wave cutoff of 50 Ry was used for the wave functions. The resulting Bloch states were then mapped onto a tight-binding Hamiltonian using PAOFLOW [74–76] for subsequent calculations of the momentum-resolved spin texture and the linear-response spin polarization.

The momentum-dependent spin texture shown in the Supplemental Material, Fig. S3(c), was obtained from the expectation value of the spin operator for each Bloch state,

$$S_n(k) = \langle \psi_{nk} | \hat{\sigma} | \psi_{nk} \rangle,$$

where $\hat{\sigma} = (\sigma_x, \sigma_y, \sigma_z)$ denotes the Pauli matrices.

The current-induced spin polarization was evaluated within linear-response theory as

$$\delta S_i = \chi_{ij} E_j,$$

where χ_{ij} is the spin-response coefficient and E_j is the applied electric field. The momentum-resolved spin response was evaluated within the constant-broadening Kubo formalism, for which [77,78]

$$\chi_{ij}(k) = -\frac{e\hbar}{\pi} \sum_{nm} \frac{\Gamma^2 \mathrm{Re}[\langle \psi_{kn} | \hat{s}_i | \psi_{km} \rangle \langle \psi_{km} | \hat{v}_j | \psi_{kn} \rangle]}{[(E_F - E_{kn})^2 + \Gamma^2][(E_F - E_{km})^2 + \Gamma^2]}$$

with $\hat{s}_i = (\hbar/2)\sigma_i$, $\hat{v}_j = (1/\hbar)(\partial H / \partial k_j)$, E_F the Fermi energy, and Γ the spectral broadening. In the calculations, a 200×200 k mesh and $\Gamma = 0.02$ eV were used.

ACKNOWLEDGMENTS

The authors acknowledge helpful discussions with Cong Xiao. The research was supported by the Ministry of Science and Technology of China (Grant No. 2024YFA1410100), the National Natural Science Foundation of China (Grants No. 12474121, No. 12488101, No. 92365302, No. 12474156, No. 22325203, No. 52102336, No. 12274411, No. 12241405, and No. 52250418), the Shanxi Province Science and Technology Cooperation and Exchange Special Project (202404041101030), the Science and Technology Commission of Shanghai Municipality (Grants No. 2019SHZDZX01, No. 20QA1405100, and No. 24LZ1401000), the Cultivation Project of Shanghai Research Center for Quantum Sciences (Grant No. LZPY2024-04), the Innovation Program for Quantum Science and Technology (Grant No. 2021ZD0302500), the Basic Research Program of the Chinese Academy of

Sciences Based on Major Scientific Infrastructures (Grant No. JZHKYPT-2021-08), and the CAS Project for Young Scientists in Basic Research (Grant No. YSBR-084). L. L. acknowledges the Xiaomi Young Scholar program and the Yangyang Development Fund. H. C. is supported by a T. D. Lee scholarship. The theoretical calculations were performed at Hefei Advanced Computing Center.

The authors declare no competing interests.

DATA AVAILABILITY

The data that support the findings of this study are available from the corresponding author upon reasonable request.

[1] L. Liu, C.-F. Pai, Y. Li, H. W. Tseng, D. C. Ralph, and R. A. Buhrman, *Spin-torque switching with the giant spin Hall effect of tantalum*, Science **336**, 555 (2012).
[2] L. Liu, O. J. Lee, T. J. Gudmundsen, D. C. Ralph, and R. A. Buhrman, *Current-induced switching of perpendicularly magnetized magnetic layers using spin torque from the spin Hall effect*, Phys. Rev. Lett. **109**, 096602 (2012).
[3] A. Manchon and S. Zhang, *Theory of nonequilibrium intrinsic spin torque in a single nanomagnet*, Phys. Rev. B **78**, 212405 (2008).
[4] I. M. Miron, K. Garello, G. Gaudin, P.-J. Zermatten, M. V. Costache, S. Auffret, S. Bandiera, B. Rodmacq, A. Schuhl, and P. Gambardella, *Perpendicular switching of a single ferromagnetic layer induced by in-plane current injection*, Nature (London) **476**, 189 (2011).
[5] A. Manchon, J. Železný, I. M. Miron, T. Jungwirth, J. Sinova, A. Thiaville, K. Garello, and P. Gambardella, *Current-induced spin-orbit torques in ferromagnetic and antiferromagnetic systems*, Rev. Mod. Phys. **91**, 035004 (2019).
[6] C. Song, R. Zhang, L. Liao, Y. Zhou, X. Zhou, R. Chen, Y. You, X. Chen, and F. Pan, *Spin-orbit torques: Materials, mechanisms, performances, and potential applications*, Prog. Mater. Sci. **118**, 100761 (2021).
[7] A. Fert, R. Ramesh, V. Garcia, F. Casanova, and M. Bibes, *Electrical control of magnetism by electric field and current-induced torques*, Rev. Mod. Phys. **96**, 015005 (2024).
[8] G. Yu, P. Upadhyaya, Y. Fan, J. G. Alzate, W. Jiang, K. L. Wong, S. Takei, S. A. Bender, L.-T. Chang, Y. Jiang, M. Lang, J. Tang, Y. Wang, Y. Tserkovnyak, P. K. Amiri, and K. L. Wang, *Switching of perpendicular magnetization by spin–orbit torques in the absence of external magnetic fields*, Nat. Nanotechnol. **9**, 548 (2014).
[9] L. You, O. Lee, D. Bhowmik, D. Labanowski, J. Hong, J. Bokor, and S. Salahuddin, *Switching of perpendicularly polarized nanomagnets with spin orbit torque without an external magnetic field by engineering a tilted anisotropy*, Proc. Natl. Acad. Sci. U.S.A. **112**, 10310 (2015).
[10] Y.-W. Oh, S.-h. Chris Baek, Y. M. Kim, H. Y. Lee, K.-D. Lee, C.-G. Yang, E.-S. Park, K.-S. Lee, K.-W. Kim, G. Go, J.-R. Jeong, B.-C. Min, H.-W. Lee, K.-J. Lee, and B.-G. Park, *Field-free switching of perpendicular magnetization through spin–orbit torque in antiferromagnet/ferromagnet/ oxide structures*, Nat. Nanotechnol. **11**, 878 (2016).
[11] Y.-C. Lau, D. Betto, K. Rode, J. M. D. Coey, and P. Stamenov, *Spin–orbit torque switching without an external field using interlayer exchange coupling*, Nat. Nanotechnol. **11**, 758 (2016).
[12] S. Fukami, C. Zhang, S. DuttaGupta, A. Kurenkov, and H. Ohno, *Magnetization switching by spin–orbit torque in an antiferromagnet–ferromagnet bilayer system*, Nat. Mater. **15**, 535 (2016).
[13] A. van den Brink, G. Vermijs, A. Solignac, J. Koo, J. T. Kohlhepp, H. J. M. Swagten, and B. Koopmans, *Field-free magnetization reversal by spin-Hall effect and exchange bias*, Nat. Commun. **7**, 10854 (2016).
[14] C. K. Safeer, E. Jué, A. Lopez, L. Buda-Prejbeanu, S. Auffret, S. Pizzini, O. Boulle, I. M. Miron, and G. Gaudin, *Spin–orbit torque magnetization switching controlled by geometry*, Nat. Nanotechnol. **11**, 143 (2016).
[15] S.-h. C. Baek, V. P. Amin, Y.-W. Oh, G. Go, S.-J. Lee, G.-H. Lee, K.-J. Kim, M. D. Stiles, B.-G. Park, and K.-J. Lee, *Spin currents and spin–orbit torques in ferromagnetic trilayers*, Nat. Mater. **17**, 509 (2018).
[16] L. Liu, Q. Qin, W. Lin, C. Li, Q. Xie, S. He, X. Shu, C. Zhou, Z. Lim, J. Yu, W. Lu, M. Li, X. Yan, S. J. Pennycook, and J. Chen, *Current-induced magnetization switching in all-oxide heterostructures*, Nat. Nanotechnol. **14**, 939 (2019).
[17] W. J. Kong, C. H. Wan, X. Wang, B. S. Tao, L. Huang, C. Fang, C. Y. Guo, Y. Guang, M. Irfan, and X. F. Han, *Spin–orbit torque switching in a T-type magnetic configuration with current orthogonal to easy axes*, Nat. Commun. **10**, 233 (2019).
[18] L. Liu, C. Zhou, X. Shu, C. Li, T. Zhao, W. Lin, J. Deng, Q. Xie, S. Chen, J. Zhou, R. Guo, H. Wang, J. Yu, S. Shi, P. Yang, S. Pennycook, A. Manchon, and J. Chen, *Symmetry-dependent field-free switching of perpendicular magnetization*, Nat. Nanotechnol. **16**, 277 (2021).
[19] J.-Y. Yoon, Y. Takeuchi, R. Takechi, J. Han, T. Uchimura, Y. Yamane, S. Kanai, J. i. Ieda, H. Ohno, and S. Fukami, *Electrical mutual switching in a noncollinear-antiferromagnetic–ferromagnetic heterostructure*, Nat. Commun. **16**, 1171 (2025).
[20] C.-F. Pai, L. Liu, Y. Li, H. W. Tseng, D. C. Ralph, and R. A. Buhrman, *Spin transfer torque devices utilizing the giant spin Hall effect of tungsten*, Appl. Phys. Lett. **101**, 122404 (2012).
[21] J. Železný, H. Gao, A. Manchon, F. Freimuth, Y. Mokrousov, J. Zemen, J. Mašek, J. Sinova, and T. Jungwirth, *Spin-orbit torques in locally and globally noncentrosymmetric crystals: Antiferromagnets and ferromagnets*, Phys. Rev. B **95**, 014403 (2017).
[22] D. MacNeill, G. M. Stiehl, M. H. D. Guimaraes, R. A. Buhrman, J. Park, and D. C. Ralph, *Control of spin–orbit torques through crystal symmetry in* WTe_2/ferromagnet *bilayers*, Nat. Phys. **13**, 300 (2017).
[23] T. Nan, C. X. Quintela, J. Irwin, G. Gurung, D. F. Shao, J. Gibbons, N. Campbell, K. Song, S. Y. Choi, L. Guo, R. D. Johnson, P. Manuel, R. V. Chopdekar, I. Hallsteinsen,

T. Tybell, P. J. Ryan, J. W. Kim, Y. Choi, P. G. Radaelli, D. C. Ralph, E. Y. Tsymbal, M. S. Rzchowski, and C. B. Eom, *Controlling spin current polarization through noncollinear antiferromagnetism*, Nat. Commun. **11**, 4671 (2020).

[24] X. Chen, S. Shi, G. Shi, X. Fan, C. Song, X. Zhou, H. Bai, L. Liao, Y. Zhou, H. Zhang, A. Li, Y. Chen, X. Han, S. Jiang, Z. Zhu, H. Wu, X. Wang, D. Xue, H. Yang, and F. Pan, *Observation of the antiferromagnetic spin Hall effect*, Nat. Mater. **20**, 800 (2021).

[25] S. Hu, D.-F. Shao, H. Yang, C. Pan, Z. Fu, M. Tang, Y. Yang, W. Fan, S. Zhou, E. Y. Tsymbal, and X. Qiu, *Efficient perpendicular magnetization switching by a magnetic spin Hall effect in a noncollinear antiferromagnet*, Nat. Commun. **13**, 4447 (2022).

[26] A. Bose, N. J. Schreiber, R. Jain, D.-F. Shao, H. P. Nair, J. Sun, X. S. Zhang, D. A. Muller, E. Y. Tsymbal, D. G. Schlom, and D. C. Ralph, *Tilted spin current generated by the collinear antiferromagnet ruthenium dioxide*, Nat. Electron. **5**, 267 (2022).

[27] M. Patton, G. Gurung, D. F. Shao, G. Noh, J. A. Mittelstaedt, M. Mazur, J. W. Kim, P. J. Ryan, E. Y. Tsymbal, S. Y. Choi, D. C. Ralph, M. S. Rzchowski, T. Nan, and C. B. Eom, *Symmetry control of unconventional spin–orbit torques in* IrO_2, Adv. Mater. **35**, 2301608 (2023).

[28] Y. Liu, G. Shi, D. Kumar, T. Kim, S. Shi, D. Yang, J. Zhang, C. Zhang, F. Wang, S. Yang, Y. Pu, P. Yu, K. Cai, and H. Yang, *Field-free switching of perpendicular magnetization at room temperature using out-of-plane spins from* $TaIrTe_4$, Nat. Electron. **6**, 732 (2023).

[29] Y. Zhang, H. Xu, K. Jia, G. Lan, Z. Huang, B. He, C. He, Q. Shao, Y. Wang, M. Zhao, T. Ma, J. Dong, C. Guo, C. Cheng, J. Feng, C. Wan, H. Wei, Y. Shi, G. Zhang, X. Han, and G. Yu, *Room temperature field-free switching of perpendicular magnetization through spin-orbit torque originating from low-symmetry type II Weyl semimetal*, Sci. Adv. **9**, eadg9819 (2023).

[30] M. Dc *et al.*, *Observation of anti-damping spin–orbit torques generated by in-plane and out-of-plane spin polarizations in* $MnPd_3$, Nat. Mater. **22**, 591 (2023).

[31] C. Cao, S. Chen, R.-C. Xiao, Z. Zhu, G. Yu, Y. Wang, X. Qiu, L. Liu, T. Zhao, D.-F. Shao, Y. Xu, J. Chen, and Q. Zhan, *Anomalous spin current anisotropy in a noncollinear antiferromagnet*, Nat. Commun. **14**, 5873 (2023).

[32] F. Wang, G. Shi, K.-W. Kim, H.-J. Park, J. G. Jang, H. R. Tan, M. Lin, Y. Liu, T. Kim, D. Yang, S. Zhao, K. Lee, S. Yang, A. Soumyanarayanan, K.-J. Lee, and H. Yang, *Field-free switching of perpendicular magnetization by two-dimensional* $PtTe_2/WTe_2$ *van der Waals heterostructures with high spin Hall conductivity*, Nat. Mater. **23**, 768 (2024).

[33] L. Bainsla, B. Zhao, N. Behera, A. M. Hoque, L. Sjöström, A. Martinelli, M. Abdel-Hafiez, J. Åkerman, and S. P. Dash, *Large out-of-plane spin–orbit torque in topological Weyl semimetal* $TaIrTe_4$, Nat. Commun. **15**, 4649 (2024).

[34] Y. Pu, G. Shi, Q. Yang, D. Yang, F. Wang, C. Zhang, and H. Yang, *Field-free switching of perpendicular magnetization by anisotropic spin Hall effect in* Mn_3Ir, Adv. Funct. Mater. **34**, 2400143 (2024).

[35] Y. F. Yang, S. Lee, Y. C. Chen, Q. Jia, B. Dixit, D. Sousa, M. Odlyzko, J. Garcia-Barriocanal, G. C. Yu, G. Haugstad, Y. H. Fan, Y. H. Huang, D. Lyu, Z. Cresswell, S. Liang, O. J. Benally, T. Low, and J. P. Wang, *Large spin-orbit torque with multi-directional spin components in* Ni_4W, Adv. Mater. **37**, 2416763 (2025).

[36] I. H. Kao, R. Muzzio, H. Zhang, M. Zhu, J. Gobbo, S. Yuan, D. Weber, R. Rao, J. Li, J. H. Edgar, J. E. Goldberger, J. Yan, D. G. Mandrus, J. Hwang, R. Cheng, J. Katoch, and S. Singh, *Deterministic switching of a perpendicularly polarized magnet using unconventional spin–orbit torques in* WTe_2, Nat. Mater. **21**, 1029 (2022).

[37] G. M. Stiehl, R. Li, V. Gupta, I. E. Baggari, S. Jiang, H. Xie, L. F. Kourkoutis, K. F. Mak, J. Shan, R. A. Buhrman, and D. C. Ralph, *Layer-dependent spin-orbit torques generated by the centrosymmetric transition metal dichalcogenide* β-$MoTe_2$, Phys. Rev. B **100**, 184402 (2019).

[38] H. Bai, L. Han, X. Y. Feng, Y. J. Zhou, R. X. Su, Q. Wang, L. Y. Liao, W. X. Zhu, X. Z. Chen, F. Pan, X. L. Fan, and C. Song, *Observation of spin splitting torque in a collinear antiferromagnet* RuO_2, Phys. Rev. Lett. **128**, 197202 (2022).

[39] S. N. Kajale, T. Nguyen, N. T. Hung, M. D. Li, and D. Sarkar, *Field-free deterministic switching of all-van der Waals spin-orbit torque system above room temperature*, Sci. Adv. **10**, eadk8669 (2024).

[40] M.-G. Kang, S. Lee, and B.-G. Park, *Field-free spin-orbit torques switching and its applications*, npj Spintron. **3**, 8 (2025).

[41] P. M. Haney, H.-W. Lee, K.-J. Lee, A. Manchon, and M. D. Stiles, *Current induced torques and interfacial spin-orbit coupling: Semiclassical modeling*, Phys. Rev. B **87**, 174411 (2013).

[42] V. P. Amin, J. Zemen, and M. D. Stiles, *Interface-generated spin currents*, Phys. Rev. Lett. **121**, 136805 (2018).

[43] See Supplemental Material at http://link.aps.org/supplemental/10.1103/gzp7-1nvx for additional information on theorical calculations, XRD, STEM, more switching measurements, orientation-dependent magnetic properties and resistivity, AHE loop shifts, HHV measurements, reversal mode of the magnetization, threshold current behavior, and domain-wall type, and mediated magnetization switching, which includes Refs. [44–56].

[44] A. J. Francis and P. A. Salvador, *Chirally oriented heteroepitaxial thin films grown by pulsed laser deposition: Pt (621) on* $SrTiO_3$ *(621)*, J. Appl. Phys. **96**, 2482 (2004).

[45] L. Chen, K. Zhang, B. Li, B. Hong, W. Huang, Y. He, X. Feng, Z. Zhang, K. Lin, W. Zhao, and Y. Zhang, *Engineering symmetry breaking enables efficient bulk spin-orbit torque-driven perpendicular magnetization switching*, Adv. Funct. Mater. **34**, 2308823 (2023).

[46] X. Shu, L. Liu, J. Zhou, W. Lin, Q. Xie, T. Zhao, C. Zhou, S. Chen, H. Wang, J. Chai, Y. Ding, W. Chen, and J. Chen, *Field-free switching of perpendicular magnetization induced by longitudinal spin-orbit-torque gradient*, Phys. Rev. Appl. **17**, 024031 (2022).

[47] C. Li, R. Xu, Y. Duan, X. Zhang, D. Zhu, A. Du, Z. Peng, S. Wang, K. Shi, and W. Zhao, *Unraveling spin–orbit torque-induced multistate magnetization switching in*

Co/Gd ferrimagnetic multilayers for physically unclonable functions, Nanoscale **17**, 8016 (2025).

[48] H. Horiuchi, Y. Araki, Y. K. Wakabayashi, J. i. Ieda, M. Yamanouchi, Y. Sato, S. Kaneta-Takada, Y. Taniyasu, H. Yamamoto, Y. Krockenberger, M. Tanaka, and S. Ohya, *Single-layer spin-orbit-torque magnetization switching due to spin berry curvature generated by minute spontaneous atomic displacement in a Weyl oxide*, Adv. Mater. **37**, 2416097 (2025).

[49] A. K. Jana, K. J. Lee, S. Lee, X. Liu, M. Dobrowolska, and J. K. Furdyna, *Magnetization switching by spin-orbit torque in crystalline (Ga, Mn) (As, P) film deposited on a vicinal GaAs substrate*, Phys. Rev. B **110**, 054422 (2024).

[50] T. Zhang, C. Wan, and X. Han, *Threshold current of field-free perpendicular magnetization switching using anomalous spin-orbit torque*, Phys. Rev. B **108**, 014432 (2023).

[51] Y. Song, Z. Dai, L. Liu, J. Wu, T. Li, X. Zhao, W. Liu, and Z. Zhang, *Field-free spin-orbit torque switching of perpendicular magnetization by making full use of spin Hall effect*, Adv. Electron. Mater. **9**, 2200987 (2022).

[52] V. K. Joshi, P. Barla, S. Bhat, and B. K. Kaushik, *From MTJ device to hybrid CMOS/MTJ circuits: A review*, IEEE Access **8**, 194105 (2020).

[53] D. Zhu and W. Zhao, *Threshold current density for perpendicular magnetization switching through spin-orbit torque*, Phys. Rev. Appl. **13**, 044078 (2020).

[54] S. Shi, J. Li, C. H. Hsu, K. Lee, Y. Wang, L. Yang, J. Wang, Q. Wang, H. Wu, W. Zhang, G. Eda, G. Liang, H. Chang, and H. Yang, *Observation of the out-of-plane polarized spin current from CVD grown* WTe_2, Adv. Quantum Technol. **4**, 2100038 (2021).

[55] M. Kuepferling, A. Casiraghi, G. Soares, G. Durin, F. Garcia-Sanchez, L. Chen, C. H. Back, C. H. Marrows, S. Tacchi, and G. Carlotti, *Measuring interfacial Dzyaloshinskii-Moriya interaction in ultrathin magnetic films*, Rev. Mod. Phys. **95**, 015003 (2023).

[56] B. Shen, M. Yang, P. Yu, S. Xu, S. Gong, and J. Luo, *Spin–orbit torque induced Néel and Bloch domain wall motion in synthetic antiferromagnets*, Jpn. J. Appl. Phys. **64**, 04SP54 (2025).

[57] X. Qiu, W. Legrand, P. He, Y. Wu, J. Yu, R. Ramaswamy, A. Manchon, and H. Yang, *Enhanced spin-orbit torque via modulation of spin current absorption*, Phys. Rev. Lett. **117**, 217206 (2016).

[58] C.-F. Pai, M. Mann, A. J. Tan, and Geoffrey S. D. Beach, *Determination of spin torque efficiencies in heterostructures with perpendicular magnetic anisotropy*, Phys. Rev. B **93**, 144409 (2016).

[59] M.-G. Kang, J.-G. Choi, J. Jeong, J. Y. Park, H.-J. Park, T. Kim, T. Lee, K.-J. Kim, K.-W. Kim, J. H. Oh, D. D. Viet, J.-R. Jeong, J. M. Yuk, J. Park, K.-J. Lee, and B.-G. Park, *Electric-field control of field-free spin-orbit torque switching via laterally modulated Rashba effect in* $Pt/Co/AlO_x$ *structures*, Nat. Commun. **12**, 7111 (2021).

[60] L. Liu, T. Moriyama, D. C. Ralph, and R. A. Buhrman, *Spin-torque ferromagnetic resonance induced by the spin Hall effect*, Phys. Rev. Lett. **106**, 036601 (2011).

[61] R. Thompson, J. Ryu, G. Choi, S. Karube, M. Kohda, J. Nitta, and B.-G. Park, *Anisotropic spin-orbit torque through crystal-orientation engineering in epitaxial Pt*, Phys. Rev. Appl. **15**, 014055 (2021).

[62] T. Ikebuchi, Y. Shiota, T. Ono, K. Nakamura, and T. Moriyama, *Crystal orientation dependence of spin Hall angle in epitaxial* Pt/FeNi *systems*, Appl. Phys. Lett. **120**, 072406 (2022).

[63] S. Emori, U. Bauer, S.-M. Ahn, E. Martinez, and G. S. D. Beach, *Current-driven dynamics of chiral ferromagnetic domain walls*, Nat. Mater. **12**, 611 (2013).

[64] S. Emori, E. Martinez, K.-J. Lee, H.-W. Lee, U. Bauer, S.-M. Ahn, P. Agrawal, D. C. Bono, and Geoffrey S. D. Beach, *Spin Hall torque magnetometry of Dzyaloshinskii domain walls*, Phys. Rev. B **90**, 184427 (2014).

[65] E. Jué, C. K. Safeer, M. Drouard, A. Lopez, P. Balint, L. Buda-Prejbeanu, O. Boulle, S. Auffret, A. Schuhl, A. Manchon, I. M. Miron, and G. Gaudin, *Chiral damping of magnetic domain walls*, Nat. Mater. **15**, 272 (2016).

[66] Q. Liu, L. Liu, G. Xing, and L. Zhu, *Asymmetric magnetization switching and programmable complete Boolean logic enabled by long-range intralayer Dzyaloshinskii-Moriya interaction*, Nat. Commun. **15**, 2978 (2024).

[67] C. Cao, Y. Wang, Y. Wang, and L. You, *Efficient spin transmission of Ti spacer for magnetic heterostructures with perpendicular magnetic anisotropy*, Appl. Phys. Lett. **126**, 262401 (2025).

[68] C. O. Avci, C.-H. Lambert, G. Sala, and P. Gambardella, *Chiral coupling between magnetic layers with orthogonal magnetization*, Phys. Rev. Lett. **127**, 167202 (2021).

[69] P. P. J. Haazen, E. Murè, J. H. Franken, R. Lavrijsen, H. J. M. Swagten, and B. Koopmans, *Domain wall depinning governed by the spin Hall effect*, Nat. Mater. **12**, 299 (2013).

[70] N. Umetsu, M. Quinsat, S. Hashimoto, T. Kondo, and M. Kado, *Spin orbit torque-driven motion of quasi-Bloch domain wall in perpendicularly magnetized W/CoFeB/MgO structure*, J. Magn. Magn. Mater. **614**, 172738 (2025).

[71] P. Giannozzi *et al.*, *QUANTUM ESPRESSO: A modular and open-source software project for quantum simulations of materials*, J. Phys. Condens. Matter **21**, 395502 (2009).

[72] D. Vanderbilt, *Soft self-consistent pseudopotentials in a generalized eigenvalue formalism*, Phys. Rev. B **41**, 7892 (1990).

[73] J. P. Perdew, K. Burke, and M. Ernzerhof, *Generalized gradient approximation made simple*, Phys. Rev. Lett. **77**, 3865 (1996).

[74] F. T. Cerasoli, A. R. Supka, A. Jayaraj, M. Costa, I. Siloi, J. Sławińska, S. Curtarolo, M. Fornari, D. Ceresoli, and M. Buongiorno, *Nardelli, Advanced modeling of materials with PAOFLOW2.0: New features and software design*, Comput. Mater. Sci. **200**, 110828 (2021).

[75] L. A. Agapito, A. Ferretti, A. Calzolari, S. Curtarolo, and M. Buongiorno, *Nardelli, Effective and accurate representation of extended Bloch states on finite Hilbert spaces*, Phys. Rev. B **88**, 165127 (2013).

[76] L. A. Agapito, S. Ismail-Beigi, S. Curtarolo, M. Fornari, and M. B. Nardelli, *Accurate tight-binding Hamiltonian*

matrices from ab initio calculations: Minimal basis sets, Phys. Rev. B **93**, 035104 (2016).

[77] F. Freimuth, S. Blügel, and Y. Mokrousov, *Spin-orbit torques in* Co/Pt(111) *and* Mn/W(001) *magnetic bilayers from first principles*, Phys. Rev. B **90**, 174423 (2014).

[78] H. Li, H. Gao, L. P. Zârbo, K. Výborný, X. Wang, I. Garate, F. Doğan, A. Čejchan, J. Sinova, T. Jungwirth, and A. Manchon, *Intraband and interband spin-orbit torques in noncentrosymmetric ferromagnets*, Phys. Rev. B **91**, 134402 (2015).